Health Control of Tree Trunk Utilizing Microwave Imaging and Reverse Problem Algorithms

Adam R. H. Alhawari, Tale Saeidi,* Idris Ismail, Turki Alsuwian, and Ahmed Jamal Abdullah Al-Gburi

Read Online

ACCESS | Metrics & More | Article Recommendations

ABSTRACT: The voids in their trunk significantly affect tropical trees' health. Both the wood and timber industries may face substantial financial losses because of the lack of an effective technique to inspect the defected trees through deep zonal monitoring. Microwave imaging offers the advantages of mobility, processing time, compactness, and resolution over alternative imaging methods. An ultra-wide band (UWB) imaging system consisting of UWB antennas and a reverse problem algorithm is proposed. Several conditions, such as the size of trunk samples (16−30 cm), number of targets, size of voids, heterogeneity of media, and number of layers, are considered in experimental studies. Based on these studies, cylindrical wooden models with 100 and 140 mm diameters, one void at the center, and three voids in different locations were 3D printed. After proving the system's ability through simulation and measurements on 3D models, a rubber-wood trunk with a length of 75 cm was cut into smaller pieces. The images created utilizing the measured data showed that the system could detect voids in the rubber trunk. Furthermore, the system indicated a high percentage of reliability and repeatability.
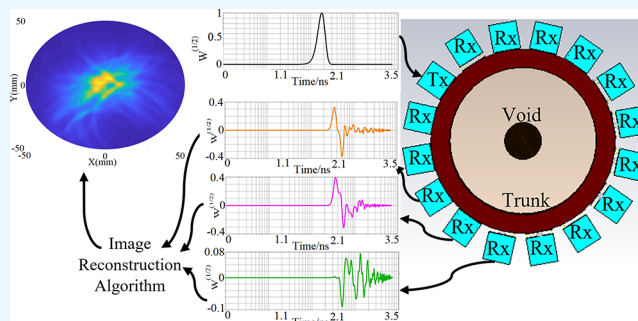
1. INTRODUCTION

Rubber trees are vital for the economy of tropical countries. One of the problems that the farmers face is the fungal disease that attacks their fruits and tree trunk.[1−6] As the dryness progresses, voids are shaped inside the stem. In addition, holes are usually shaped in a trunk when aridity increases. For a deep inspection of a field, unmanned aerial vehicles (UAVs) may be utilized to monitor the evident symptoms of destruction.[7] However, UAVs cannot check for any internal defects. Hence, other solutions were suggested to perform the monitoring process more deeply with minimally invasive methods and minor side effects, such as applying chemicals.[8,9] The nondestructive testing (NDT) technique was recommended for the internal inspection of materials, trees, and organs with a noninvasive method with minimal environmental effect. Tomography methods, for instance, can be a reliable alternative to examining trees. These methods have been employed to generate a cross-sectional image of a subject using light waves or electromagnetic waves.[10]

Some tomographic systems utilize probes located around dense areas such as rubberwood trunks. The ultrasound (US) method offers low-to-medium-resolution images because sound waves cannot travel straight in such asymmetrical and dense materials. Therefore, localizing the voids inside wood using the US is not easy. In addition, the US cannot discriminate between a particular void and a group of other voids since the transmit time resulting from the damage near

the surface can be similar to the more profound damage.[10−12] Other techniques introduced insufficient spatial resolution. High-resolution X-ray computed tomography (HRXCT) takes a long time to process and may cause danger to the environment and the operator. They are very dependent on the density of the material and its distance from the sample. In addition, Gamma computed tomography (CT) may be used, but it is unsafe for the environment, needs a long processing time, and poses immobility issues.[13,14]

A different method is needed to overcome the challenges mentioned. Microwave tomography (MT) is a nondestructive method that may also provide safety while it has the advantages of being low cost, portable, and requiring low processing time.
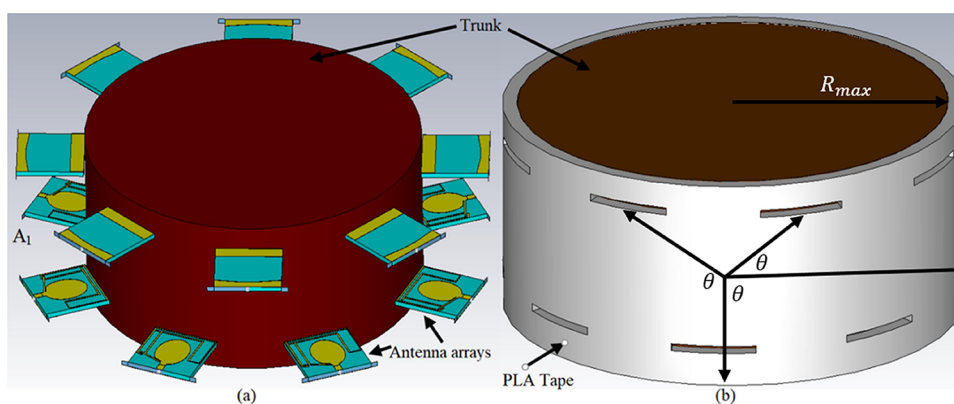
Microwave imaging (MWI) approaches are currently present and employed in various fields.[15] Dielectric characteristic extraction and target localization are two of the most common applications of MT.[16−20] For example, some studies have utilized MWI to examine rubber tree leaf dielectric

Figure 1. (a) Simulation setup along with the antenna array, (b) the trunk sample, and the elastic PLA tape.

characteristics[21] and oil palm natural rubber (the dielectric properties of oil palm/natural rubber composite materials were characterized).[22] Moreover, MWI and microwave sensing are standard methods for localization targets (also known as microwave radar imaging). MWI based on radar usually uses two or several low-power ultra-wideband pulse-like waves.[23,24]

In wood imaging, several studies were performed to identify voids in the trunk or characterize a wooden piece to distinguish hollows. The backpropagation method was carried out to create images of a hole in a trunk made of wood. Nevertheless, the achieved composed images indicated that the void could not be identified, and the images were dim because of the interferences at only a specific measured frequency.[25] The MWI structures used in these studies are complex. Also, the antennas employed in the system are enormous, where a 30-element array was used. A tedious multi-static technique was imposed when no prior knowledge of the samples under test existed.[26] Therefore, less processing time is required for the methods based on time reversal. Images were obtained with only one transmitter and multiple antenna receivers. The authors in ref 27 used a combination of backpropagation and iterative methods to recreate an image. They mechanically turned the transceiver sensors (large antennas) horizontally and vertically.[27]

Additionally, voids in agarwood were hypothetically spotted utilizing MWI. However, their performance in void detection in agarwood using six different methods could not identify the target clearly, and their quality of estimating the structural similarity index (SSI) was not sufficient (it was less than 47%).[28] Consequently, a system having an efficient and short processing time for image reconstruction that can create high precision is necessary.

An antenna array configuration is needed for constructing images using the MWI method. UWB antennas can provide better resolution images since they offer wider BW and use these broad BW and the received pulses. Therefore, they can provide more spatial resolution. They can also help recognize the desired target near some other adjacent elements. Commonly, a planar or a cylindrical arrangement is used. The planar array was primarily applied to validate the imaging methods and antenna array performances[24] and other purposes.[29,30] A cylindrical array is the most suitable arrangement for MWI in wood imaging due to the cylindrical shape of the tree trunk. A more experimental assessment is presented in this paper. The actual rubber trunk sample is utilized as a sample and imaging environment, not just simulation and 3D-printed models.[31] The reconstructed

images from the experimental trunk show that the proposed system can detect the voids in a realistic scenario.

2. IMAGING METHOD

In this section, a brief background on the MWI methods is presented. Three methods of MWI exist: (1) passive, (2) hybrid, and (3) active methods. The passive method works based on microwave heating and creates images based on the object's temperature under test (OUT). Microwave and acoustic waves are combined in the hybrid method. The active MWI technique works based on the difference in the electric characteristics between the healthy and defective areas of different materials.[32] The active MWI techniques can be divided into two categories. MT uses the scattered collected fields around the object, and the images are created by solving an inverse problem. MT radar imaging is based on the backscattering of the waves. It can create an image of regions of different materials inside OUT boundaries using the time of arrival of the reflected waves. Most active MWI systems use UWB transceivers. In these systems, UWB antennas send and receive UWB pulses in the time domain or use multiple frequencies within the UWB band to send time-harmonic signals. The use of wide bandwidth is necessary to provide high-resolution images. The reflected, transmitted, and scattered signals are collected by the UWB antennas, digitized, and used in different imaging algorithms to recreate and reconstruct the target image. The scatterers (voids) and the surrounding areas cause scattering and show extra energy levels accordingly.[33−41]

2.1. Microwave Imaging Setup for Imaging of Wooden Trunks. The focus of this study is the use of MWI to find voids inside a rubber tree trunk. In the proposed setup, the trunk sample is in contact with the UWB antenna sensors for measuring the scattered fields. A polylactic acid (PLA) elastic shell was 3D-printed to hold the antenna sensors in place during the measurements. The PLA shell and the proposed antennas for wood imaging are shown in Figure 1 (introduced in ref 24). The locations of UWB antennas were selected according to the proposed antennas' main lobes. It is mainly around 180−210° with a beamwidth of approximately 60°. Therefore, the antennas were arranged to focus the beam at the center of the trunk, although the beam can cover a larger area, and the constructed images will be shown later in the paper. Equation 1 determines the polar coordinates of the antenna with index B.

$$\gamma = R_{\max} - d_r, \theta = (B - 1)\,\pi/8 \qquad (1)$$

where d_r is the radial distance between two array elements, θ is the angle between every transmitter and receiver, and R_{max} is the maximum diameter of the trunk sample (the d_r is needed later to calculate the delay time that signal takes to get to an antenna from another array).

Sixteen antenna elements were used to excite the sample and collect the scattering data. Each antenna has an area of $20 \times 20 \times 1.5$ mm^3.[24] The arrangement of the antenna elements around the sample under test is shown in Figure 1a. Since the antenna is small, we could arrange eight antennas around the wood sample in each row. It is essential since having more antennas can provide more scattering data sampling points, and therefore, more accuracy can be attained accordingly.[33] The proposed antenna uses a substrate with $\varepsilon_r = 2.55$, which is close to the dielectric constant of most wood types, such as dry wood, plywood, and rubber wood, in a dry condition. Since the dielectric constant difference between the antenna's substrate and OUT is small, reflections at the surface are negligible and can be ignored. The proposed UWB antenna's characteristics and working capability in wood media were studied and presented for a planar configuration.[24] This study will examine its ability to work in a cylindrical arrangement.

2.2. Electromagnetic Fields and Inverse Problems.
Several imaging algorithms are in the form of inverse problems. For example, inverse scattering algorithms can be used to reconstruct an image. One of these algorisms is the time-reversal algorithm which applies the Wave Equation's reciprocal properties. The electric (E) and magnetic (H) fields are backpropagated to concentrate the field at the target. The receiver and transmitter antenna elements applied in a time-reversal approach are mirrors. The time-reversal algorithm has been utilized for various applications, such as ultrasound imaging.[42] It performed well in heterogeneous and dense environments.[43−47] The time-reversal algorithm is a promising imaging method since it provides high-accuracy outcomes; however, it is challenging due to its wide bandwidth and high-fidelity value requirements. The fidelity values should be low to keep the signal distortion at an acceptable level, and how the received signals are similar in shape.

Moreover, it indicates the similarity of the received signals too. Also, the choice of the transmitted signal should be such that a high correlation with the scattered field is present.[48,49] The time-reversal method can be implemented using a Finite Integration Technique (FIT).[31] In this study, the simulation and modeling were carried out in CST Microwave Studio 2020. The modeling area consists of the UWB antennas and the trunk sample inside the radiation boundaries. When Maxwell's equations are solved using FIT, the fields are reversed in time and backscattered.[50] It should be mentioned that a modulated Gaussian pulse is used as antenna sensors' input using eq 2 ($f_r = 0.9$ GHz, ω is the pulse width) (Figure 2).

$$S(t) = e^{-(t-t_0)^2/2\omega^2}\cos(2\pi f_r t) \qquad (2)$$

The transmitted fields should be subtracted from the total field to show the effects of the voids on each received signal. Therefore, the received signals with and without OUT are collected. The total received signals with and without OUT are shown in Figure 3, assuming that antenna A$_1$ is the transmitter and A$_2$−A$_{16}$ is the receiver. The received signals are attained when antennas are located around the trunk sample. They are
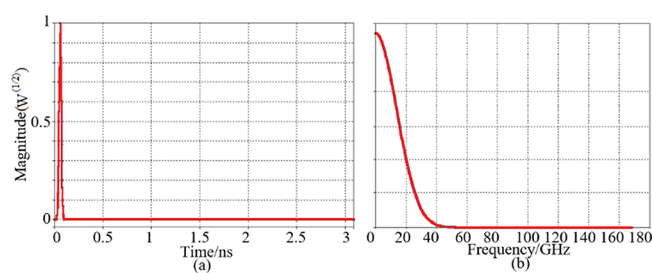

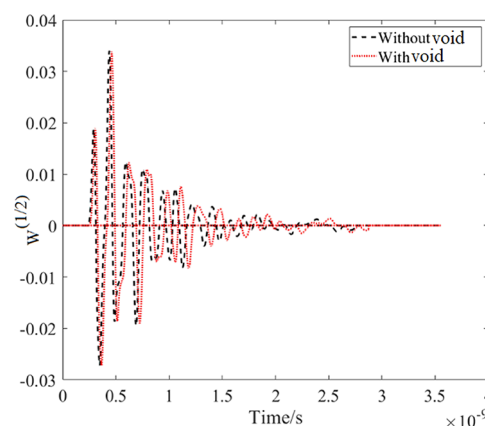**Figure 2.** (a) Gaussian pulse, (b) the UWB pulse response.

Figure 3. Total received signals.

put on a cylinder with a radius of 50 mm. A void is placed at the center of the cylinder with a radius of 4 mm.
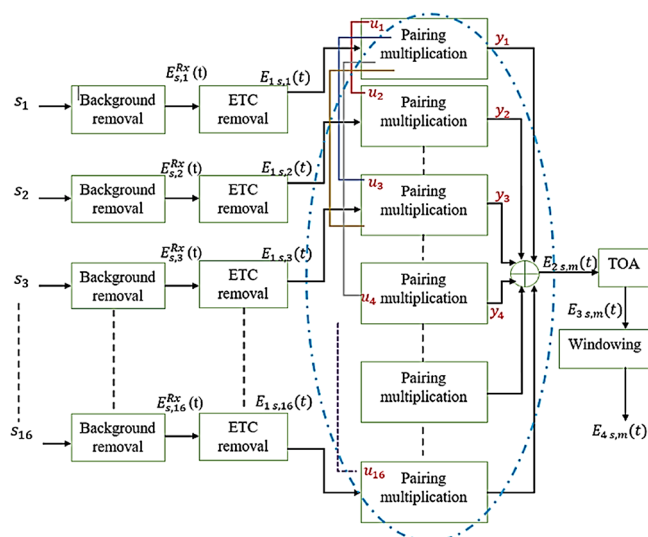
3. IMAGE RECONSTRUCTION AND DETECTION OF VOIDS IN THE TRUNK SAMPLES

In our previous work, we designed and tested a microwave imaging system with ten antenna elements arranged in a planar lattice to check their radiating efficiency in the vicinity of wood and their capability in wood void imaging.[24] This study presents a cylindrical array of 16 antenna elements arranged around the PLA-printed samples representing a rubberwood trunk piece model. The considered trunk sample had a 100 mm diameter and 55 mm thickness (height). The reason behind choosing this diameter is to detect voids at an early stage and when the rubber trees are young. Furthermore, the dielectric properties of the tree trunk are presented in ref 51. The dielectric constant for a healthy part when the rubber tree trunk has a moisture content (MC) of 10% is between 5 and 7.

On the other hand, the defective part of the trunk is considered almost completely dry. Therefore, it has a dielectric constant of around 3. Thus, the dielectric constant was assumed during the simulation, and the image processing was within 3−7.[51]

Signals are time-reversed and then backpropagated to the trunk to concentrate on the focal point in this imaging area (it is backpropagated to every point in the trunk). It is to start the image reconstruction of the void in the trunk sample. It is done to obtain and extract the void response and differentiate it from the other undesired signals, like other parts of the trunk. The other antenna elements' clutters, noise, and mutual effects. The effect of clutters should be suppressed or removed to improve the signal-to-noise ratio. Otherwise, they will have a dominant influence on the void response. An algorithm is proposed in detail in ref 31 and a block diagram of it is shown

in Figure 4 to remove the clutter and artifact effects and modify the void's response. We applied this algorithm to

Figure 4. Applied algorithm for image reconstruction of voids in the trunk (ETC: early time content, TOA: time of arrival) (u and y are the input and output of the paring multiplication).

construct the void's image. We then compared the results with filtered delay multiply and sum (FDMAS) and modified weighted delay and sum (MWDAS) algorithms for comparison and evaluation.

When the proposed algorithm presented in ref 31 was applied, the received signals shown as s1−s16 in Figure 4 were imported into the program. Then, the output of each part, as shown in Figure 4, was calculated. Figure 5 shows the output and received signal amplitude after each image reconstruction stage. The early time and unwanted late time content are

suppressed after each phase. The output is therefore focused on showing the void's response. The clutters and artifacts are removed after applying each step.

4. RESULTS AND DISCUSSION

The critical parameters affecting the image reconstruction of the void in the cylindrical configuration should be investigated before starting the imaging of the sample (these parameters were already evaluated in a planar setup[24]). These parameters are the received signals, coupling effects of the antenna arrays, and the fidelity factor. Figure 6 depicts these parameters for a sixteen-element cylindrical setup around the rubber tree trunk and its void through simulation.

Figure 7 displays the signals received from six antenna elements (A_2, A_5, A_9, A_{11}, A_{14}, and A_{16}) when the array transmits and receives signals imaging a healthy or defective sample. A slight shift in signals is noticed. It could be due to the different locations and distances between each antenna and the void. The delay occurs when the signals reach the receivers. However, it can be observed that the signals' shapes are the same, and only the peak is shifted. The fidelity factor is how we can evaluate and investigate the similarity of the received signals and the level of the signal's distortion. The fidelity percentage is depicted in Figure 8, which was more than 90% in both cases of imaging void-free and defective samples. Equations 17 and 18 in ref 52 show the fidelity formula, and they can be used to calculate the fidelity factor (FF) using the simulated and measured signals.

$$F = \max \int_{-\infty}^{+\infty} \mathrm{x}{\sim}(t) \cdot \mathrm{y}{\sim}(t - \tau) \mathrm{d}t \tag{3}$$
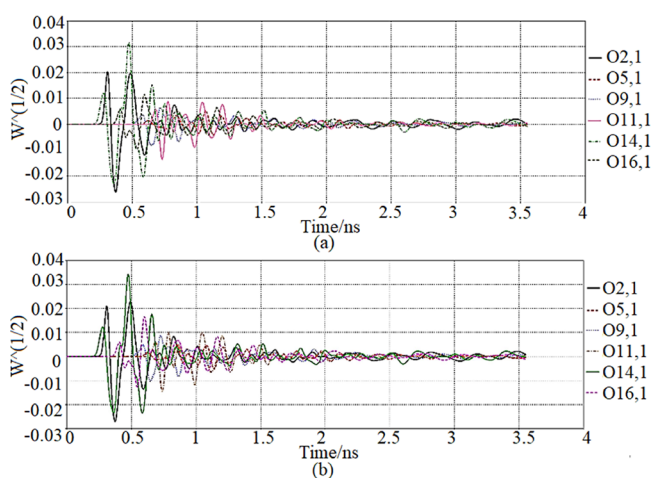
where $\mathrm{x}{\sim}(t) = \dfrac{x(t)}{\sqrt{\int_{-\infty}^{+\infty} |x(t)^2| \, dt}}$, $\mathrm{y}{\sim}(t) = \dfrac{y(t)}{\sqrt{\int_{-\infty}^{+\infty} |y(t)^2| \, dt}}$; τ is the shifted time, and F is assumed as the maximum cross-
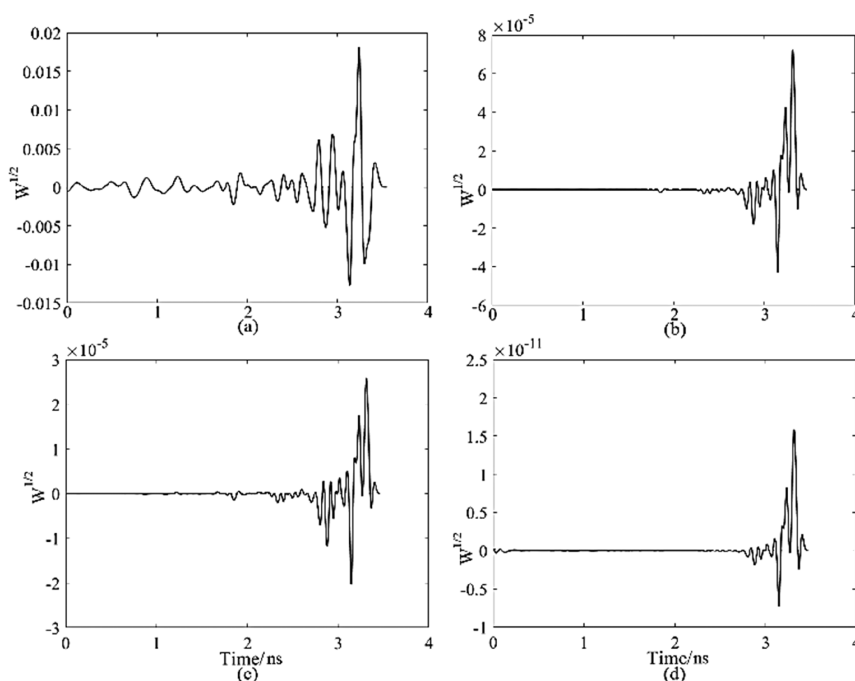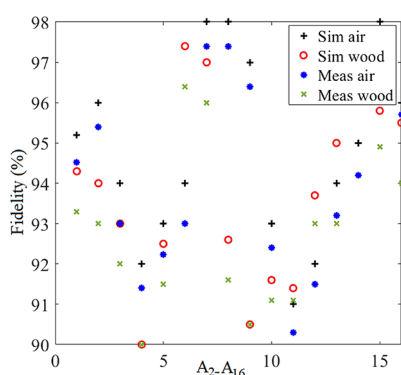

Figure 5. Received pulses after each stage of imaging (a) background reduction (E^{Rx}), (b) early time content removal (E_1), (c) time of arrival (E_3), and (d) windowing (E_4).
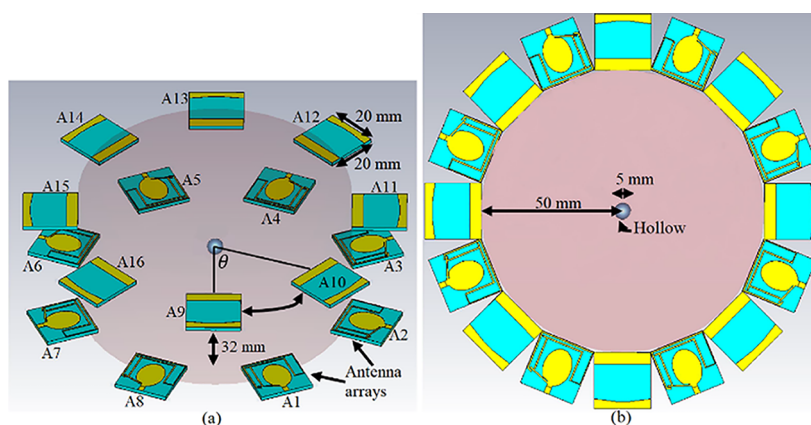
Figure 6. Antenna arrays around the wood trunk; (a) 3D view and (b) 2D view.

Figure 7. Received signals from various antenna elements for the (a) void-free sample and the (b) defected trunk sample.

Figure 8. Measured and simulated fidelity percentage of received signals in healthy and defective wood and air.

correlation function of two signals when normalized to their energy level.

FF may vary between 0 and 1, where zero shows no similarity and 1 means the maximum similarity of 100%. Since the void-free and the defective samples have different physical and electrical properties, their FF percentage is different.

A_1 sends the pulse, and other antennas around the sample are positioned at different angles to receive it. These collected data are used to acquire fidelity. First, the transmitted pulse is assumed as a reference, and its Fast Furrier Transform (FFT)

is calculated to calculate FF. Then, the other received pulses are multiplied by that. Afterward, their inverse FFT values are calculated, and their similarity percentage is compared and plotted. The following formula calculates fidelity using the previous explanation and eq 3.

$$F = \max \frac{\int_{-\infty}^{+\infty} x(t) \cdot y(t - \tau) \mathrm{d}t}{\sqrt{\int_{-\infty}^{+\infty} |x(t)|^2 |\mathrm{d}t \cdot \int_{-\infty}^{+\infty} |y(t)|^2 |\mathrm{d}t}} \tag{4}$$

In addition to FF, various antenna elements' transmission coefficients are investigated to show their coupling level. Figure 9 shows that the level of mutual coupling between antenna elements within the bandwidth is less than −20 dB.

Many parameters may affect the quality and accuracy of the images. Therefore, we have considered some variations. Some of these are the number of antenna elements, the number of voids, the dimensions, the trunk sample radii (8 and 15 cm), the number of layers, and symmetric vs asymmetric samples. Unless otherwise mentioned, a void radius of 4 mm was assumed in all the cases under study (one point of 2 mm radius). Unless otherwise noted, the trunk radius was 5 cm for all the experiments (cases of 8 and 15 cm radii).

The mutual coupling between the antenna elements was considered and investigated in the absence of the samples. The mutual coupling among the sensors influences cylindrical array characteristics. The mutual coupling was less than −20 dB over the whole band and less than −30 dB for the band of 12 to −20 GHz. It was observed that mutual coupling was affected by the distance, positions, and medium and whether the void existed. For instance, the mutual coupling between A_1 and A_5 is lower due to the larger spacing. It is also due to the impact of the void on the signal's way. This section may be divided into subheadings. It should provide a concise and precise description of the experimental results, their interpretation, and the practical conclusions that can be drawn.

Another vital factor in evaluating an imaging system's capability to detect a target is the resolution. It is a factor that describes the ability to see small targets and the resolution of the system. Three kinds of resolution exist. We used the following equations available in previous studies[53−55] and calculated spatial (D), cross-range (ΔX), and rage resolution (ρ_r) to be ∼5.5, ∼6.5, and ∼8.5 mm, respectively.[56]

$$D = \sqrt{S_{\text{imaging zone}}/r}, \ \Delta X = R \times \Delta\theta, \ \rho_r = c/(2Bw) \tag{5}$$
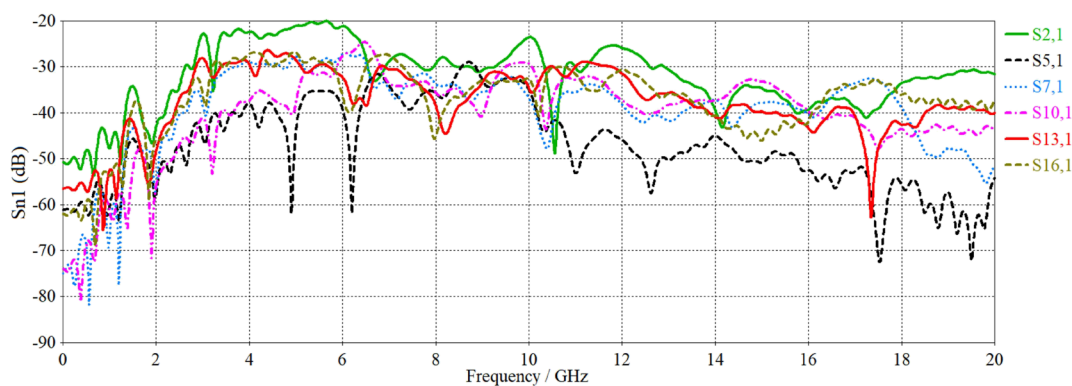
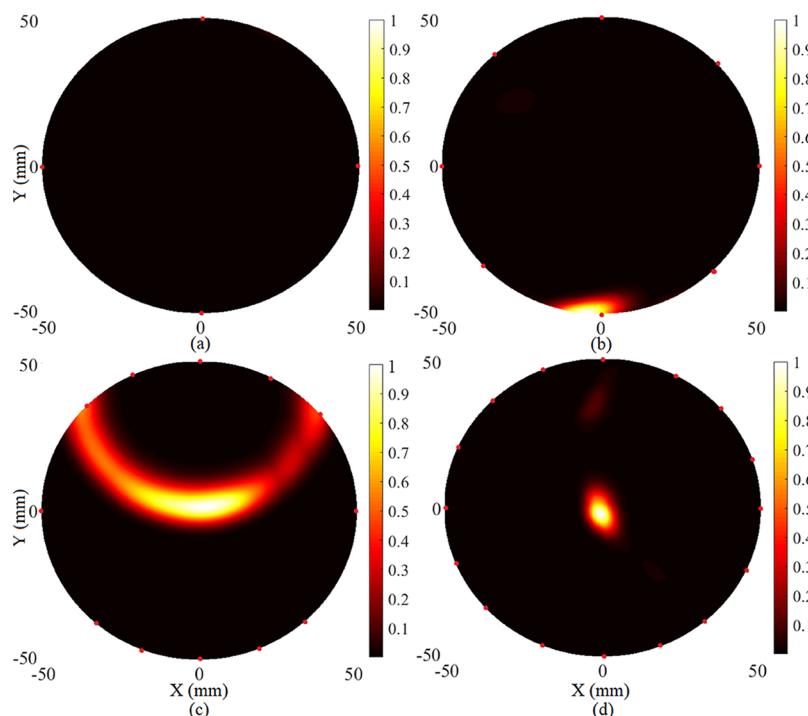**Figure 9.** Transmission coefficient results from antenna elements.

Figure 10. Reconstructed image using (d) robust TR compared with (a) MWDAS, (b) FDMAS, and (c) STR.

where R is the distance between the scatter and the radar, Bw is the adequate bandwidth of the pulse, and c is the speed of light $(2L_{eff})$. L_{eff} is the actual array length, while r denotes the effective rank that establishes the size of the reconstructed image. The number of evenly spaced points in the imaging zone is considered during picture reconstruction. The signals displayed in the flowchart in Figure 4 are all the signals used in these calculations. After data collection, the delay time, antenna placements, and distances between them were computed. The image was then rebuilt after measuring the intensity value of each focal point (the signal or field amplitude at each place inside the imaging environment). The first investigation was to reconstruct the image considering various numbers of antenna elements. Next, we assessed the system's ability to create an image of a void compared with three other algorithms, MWDAS, FDMAS, and Standard Time Reversal (STR).

4.1. Void Detection Using Simulated Signals. Figure 10 shows the reconstructed image of a void at the center created using 16 antennas around the sample and a robust

time-reversal (TR) algorithm. This constructed image is compared with images using three other algorithms MWDAS, FDMAS, and STR.[50]

By increasing the number of elements, the image precision and correctness in localizing the void increased, and the number of clusters decreased. It is due to the increased information collected by taking more samples of the scattering data. The results showed great accuracy and clutter removal. Also, applying the Robust TR (RTR) enhanced the distinction of voids at the central part (the array size has been discussed in ref 31).

Figure 11 demonstrates the recreated central void images in a larger size of the wood trunk with 16 and 30 cm diameters. The RTR algorithm achieved better clutter removal performance than the results of MWDAS, FDMAS, and STR algorithms. However, a small central minor cluttered area remained at the center. It could be avoided or improved by increasing the space between the void and antenna elements and the reflection time. Figure 10 shows the reconstructed images using the proposed Robust TR and three other
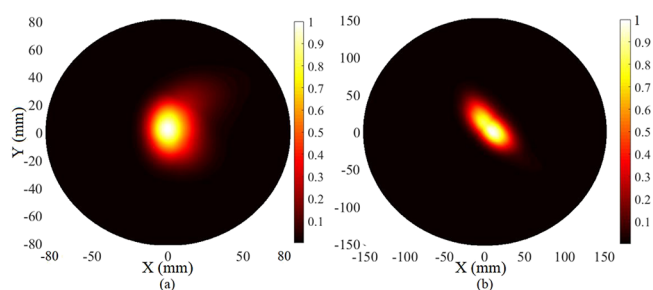
Figure 11. Recreated image of a trunk with a radius of (a) 16 and (b) 30 cm.

algorithms. It is noticed that using the proposed Robust TR, a better-reconstructed image is obtained. However, the images shown in Figures 10 and 11 and the other reconstructed images might not be symmetrical. It might be because we only use the data when one array sends and the different arrays receive to save more time. The image will be more symmetrical if we use data when all the arrays send and received at the time.

The reconstructed image of three off-center voids is depicted in Figure 12. The array system identified every three holes with
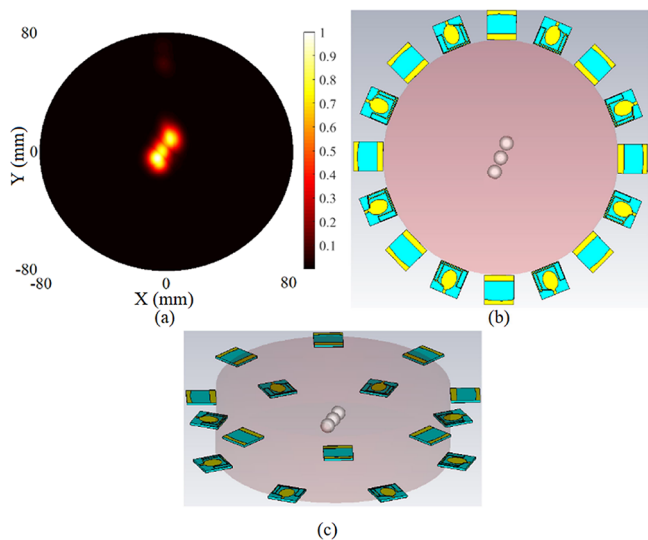
Figure 12. Reconstructed image of three voids in a simulated model of a wood trunk sample with a diameter of 16 cm (a: the reconstructed image, b: top view simulation setup, and c: perspective view of the simulation setup).

a slight error in their position (the error is presented later as MSE in Table 2). Figure 12a shows that the trunk diameter was 16 cm to show the system, and the algorithm can remove the clutters and differentiate more than one void from the surrounding clutters. The simulation setup is presented in Figure 12b,c. The space between every two targets and the diameters of these three targets are 4 and 5 mm, respectively.

When examining the system's capability in detecting the void, it is vital to consider that the tree trunk has multiple layers, like the tree's live and dead dark layers. We thought of two layers. The outer layer has a dielectric constant of 5, like a wood sample, when it has approximately 10% moisture. The central part has a higher dielectric constant (ε_r = 7) due to the higher moisture content at the central part of the rubber tree trunk (Figure 13). Despite having differences in the dielectric constants and higher moisture content, the image clearly shows
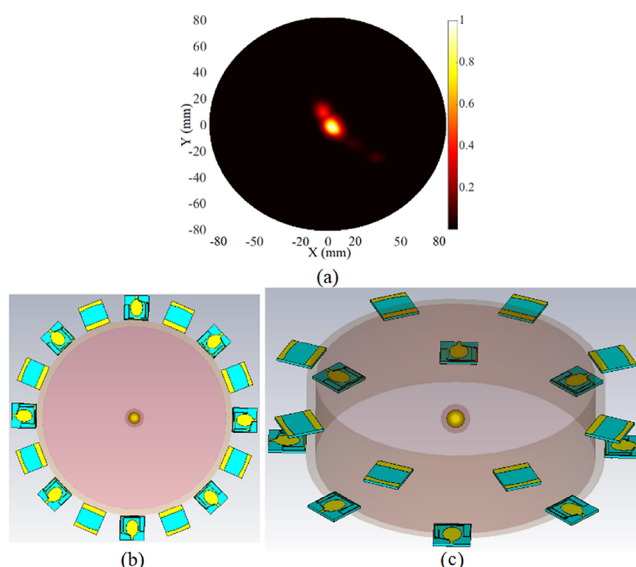
Figure 13. Reconstructed image of central hollow in the trunk wood with a diameter of 16 cm and two layers: (a) reconstructed image, (b, c) simulation setup.

the void at the center with a diameter of 5 mm. However, a few blurry areas exist around the void. This small out-of-focus area might be due to the signal reflection or scattering caused by the mismatch at the surface layers.

We then examined if the system could detect smaller voids. We chose a smaller radius of the void of 2 mm. We placed a void at the center of the sample. The sample had two layers to model the outer layer with a lower permittivity and the inner one with a higher dielectric constant. Figure 14 shows the
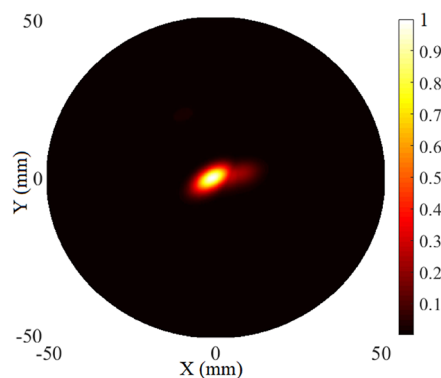
Figure 14. Reconstructed image of the hollow with a radius of 2 mm.

reconstructed image of the smaller void using the RTR algorithm.[31] Figure 15 illustrates a heterogenous trunk sample for the examination. This sample is constructed of two cylindrical shapes with the largest dimensions: X = 210 mm and Y = 160 mm. The void was at the location of X = −25 mm and Y = −5 mm. The spherical void located at this position had a radius of 2 mm. The reconstructed image clearly shows that the proposed array system identifies voids in these asymmetrical samples with the capability to remove clutter and artifacts. However, some clutters can be seen that might have been caused by the unequal distribution of antennas which affected the time delays in signals.

4.2. Void Detection Using an Experimental Setup. A measurement setup was used to test the imaging algorithm's
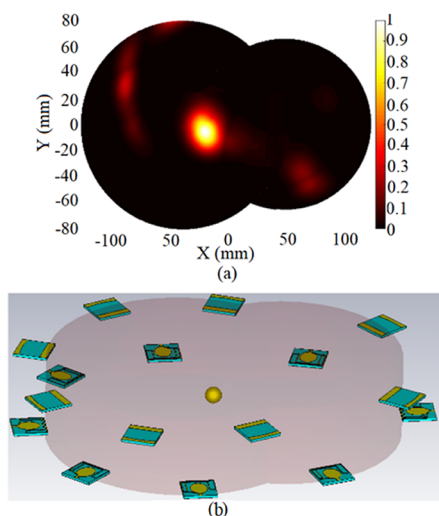
Figure 15. Reconstructed image of a void embedded in an asymmetrical wood sample (a: the reconstructed image, b: the simulation setup).

**Figure 17.** Measurement setup for the 3D-fabricated samples with a radius of 7 cm.

capability to create tree trunk images. We used 3D-printed samples that have dielectric properties similar to wood. It should be mentioned that a cube was 3D-printed to measure the dielectric constant of the material within the band of 2.45 to 3.26 GHz and to be sure that the dielectric properties stayed in the range (Figure 16). The dielectric properties measurement was carried out in the cross-section direction. We ensured that the 3D-fabricated cube had a smooth surface to reduce the impact of air gaps between the cube and the surface of the coaxial dielectric probe. Any air gaps could cause an inaccurate outcome. Figure 17 shows the 3D-printed cube and the dielectric probe calibration and measurement setup (the

measured dielectric properties of the cube are presented in Figure 17 of ref 31 and are not repeated here).

First, we prepared four symmetrical samples with 5 and 7 cm radii. These samples had no voids or defects and were used for calibration of the system (Figure 17). Additionally, two heterogeneous 3D-printed models, one representing a healthy trunk and one representing a trunk with defects with the exact outer dimensions, were prepared. The asymmetrical samples had the same dimensions as were used in the simulations (210 mm × 160 mm) (a total of six pieces). The models were 3D-printed with a material (PLA wood with 40% wood and a constant dielectric range of 2.5−3.5).[57] Also, a flexible elastic strip was printed to hold the antennas in place and wrapped around the trunk sample.
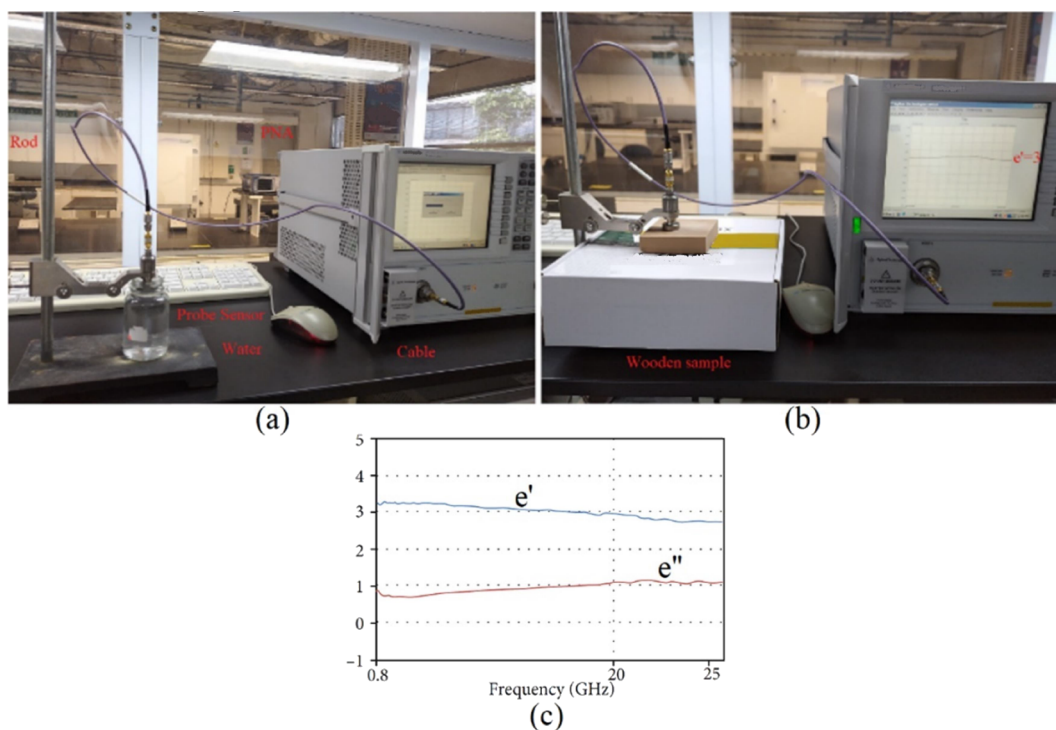

Figure 16. Measurement setup for dielectric properties measurement of a 3D-printed cube: (a) calibration, (b) measurement, (c) measurement dielectric constant (e'), and dielectric loss (e'').

In one symmetrical trunk sample, the void was located at the center. In another proportional model, the void was located at $X = -10$ mm and $Y = 0$, where the origin was the center of the cylindrical sample. The dimensions of the 3D-printed sample were $\pi (50)^2 \times 55$ mm^2 and $\pi (70)^2 \times 55$ mm^2 (π (radius)$^2 \times$ height). The void radius was 2 mm. Figure 17 shows the array with 16 antenna elements placed on two rings with a height difference of 25 mm and connected to a vector network analyzer (Performance Network Analyzer- PNA, model HP 85070-Ds) positioned around the 3D-printed sample with a radius of 7 cm.

All sixteen antenna elements ($A_1 - A_{16}$) were fabricated, soldered, assembled, and then positioned on the flexible strip, and they were fixed in their positions to ensure no movement. The measurement was performed manually (no switching network was used). The scattering parameters (reflection and transmission coefficients) were recorded for each pair of antennas ($A_1 - A_2$, ..., $A_1 - A_{16}$) and then extracted for further investigations. It should be mentioned that the PNA was carefully calibrated. Times and the scattering matrix at several frequencies were saved and utilized to produce a pulse in the time domain through IFTT. Finally, the extracted S-parameters were imported to MATLAB to perform the image reconstruction by applying RTR.

The reconstructed images for a circular void with a 2 mm radius within the fabricated samples of 5 and 7 cm radii are shown in Figure 18a,b, respectively. The images depict the location of the voids. There are a few insignificant clutters.
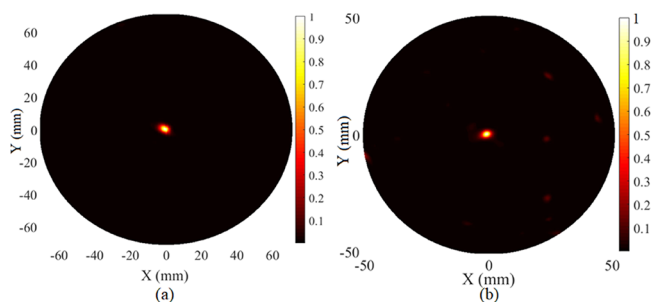

Figure 18. Recreated image applying the measured data for the fabricated sample (a: 5 cm radius and b: 7 cm radius).

Figure 19 shows the reconstructed image of the asymmetrical fabricated trunk model. The trunk model is imprinted in a rectangle with the following measurements: 210 mm, 160 mm, and a height of 55 mm (the same as what was used in the simulation). The middle of the enclosing rectangle, where $X =$
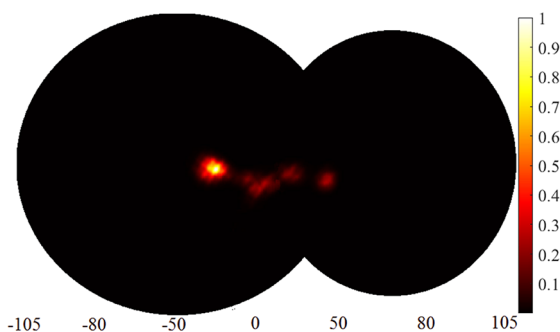
Figure 19. Reconstructed image for the asymmetric fabricated sample.

0 and $Y = 0$, is where the void is located at $X = -25$ mm, $Y = 0$ mm. The void with a radius of 2.5 mm was found and localized in the right place, as shown in Figure 20.
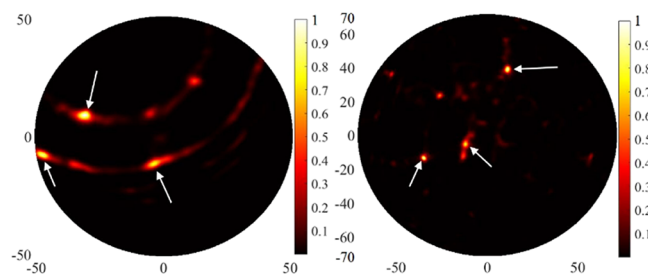

Figure 20. Reconstructed image using the measured data for three voids inside two different-size models.

After checking the system's ability of the detection of a single void in both symmetrical and asymmetrical fabricated models, four more trunk models were fabricated, each with three voids within them. All three voids had a radius of 2 mm, but they were located at three different locations within the fabricated model. The samples had radii of 50 and 70 mm. Figure 20 depicts the reconstructed image of three voids in two fabricated models. All three holes can be detected at their exact locations. However, some negligible clutters are also seen (they are insignificant compared to the actual place of the targets and their accurate shapes. Furthermore, they are recognizable compared to the tiny clutters in the imaging environment).

4.2.1. Image Reconstruction of Actual Tree Trunk Using the Experimental Data. At the final stage, after ensuring the system's capability in imaging small voids using the 3D-printed samples, a rubber-tree trunk with a length of 75 cm was obtained and used for testing the system. The model is shown in Figure 21a. Next, the large sample was cut into smaller pieces to examine how different dimensions and heterogeneity of the trunk affect the reconstructed images.

The elastic, flexible 3D-printed strip holding antennas was wrapped around the trunk piece without any air gap between the antennas and the surface of the trunk. The measurement setup was then utilized to collect the scattering data, similar to the process used for the 3D-printed samples. Two trunk pieces were used in this measurement. One model had a smaller size,
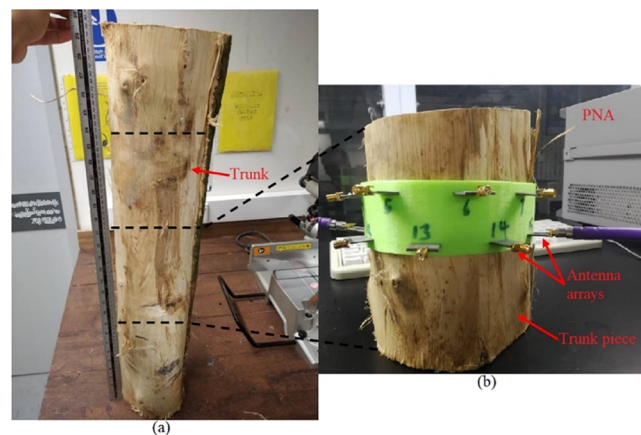

Figure 21. Measurement setup for imaging a tree trunk sample is (a) the rubber-tree trunk sample, (b) a cut piece, and the measurement setup.

inscribed in a volume with the dimensions of 190 × 185 × 20 mm³, and the other one with a larger size, cut in a volume with the dimensions of 240 × 200 × 25 mm³. It should be mentioned that the dielectric properties of the trunk were measured and used in the image reconstruction. The dielectric properties measurement was performed the same way it is presented in ref 51. The dielectric constant in the radial direction was between 3−7. It depends on the moisture content of the layers inside the trunk. Table 1 depicts the

Table 1. Dielectric Constant Ranges of the Actual Trunk (Each Layer and Different Percentages of MC)

	dielectric constant (ε_r)	
dielectric constant (ε_r)	minimum	maximum
core (10% MC)	2	5
first layer (10% MC)	3	5.5
second layer (10% MC)	5	7
complete trunk with all layers (10% MC)	5	7
20% MC	6.5	14
30% MC	9.5	17
60% MC	14	24

dielectric variations for each layer (three different layers shown in Figure 22b) and different percentages of moisture constant
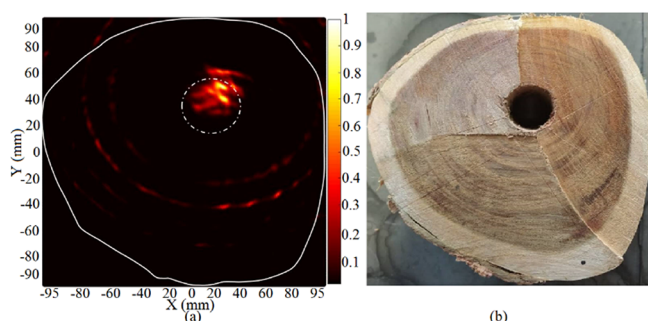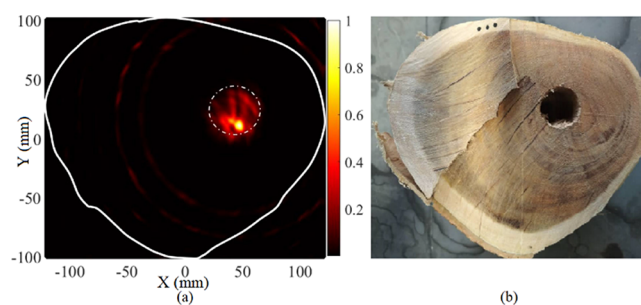

**Figure 22.** (a) Reconstructed image and (b) the smaller size trunk sample.

(MC). It also demonstrates that the dielectric constant does not alter too much between 5 and 7 when the MC is 10%. The dielectric constant was also examined, considering the different MC percentages of the trunk. The process of how the measurement was performed in various moisture levels was completely explained in ref 58, taking into consideration the time and weight of the trunk during the measurement.

Figures 22 and 23 show the reconstructed image of these two trunk pieces. It can be seen that the approximated central void has around a 6 mm radius. The accuracy in finding the location and size of the hole was excellent, although small size clutters and a slight shift in the void's location can be observed. The variability of the trunk and the antenna arrays' asymmetrical placement around the trunk may be to blame.

4.3. Structural Similarity Index. The quality of the reconstructed central images can be examined by comparing them with a reference image (Figure 24, the reference image for the central images is provided just as an example of the reference image). For example, a reference image forms a 4 mm radius sphere (2D circular surface) with a mean-squared error (MSE) of 0 and an SSI of 1 when no clutters exist. This reference image was to show how much the reconstructed

Figure 23. (a) Reconstructed image and (b) the larger size trunk sample.
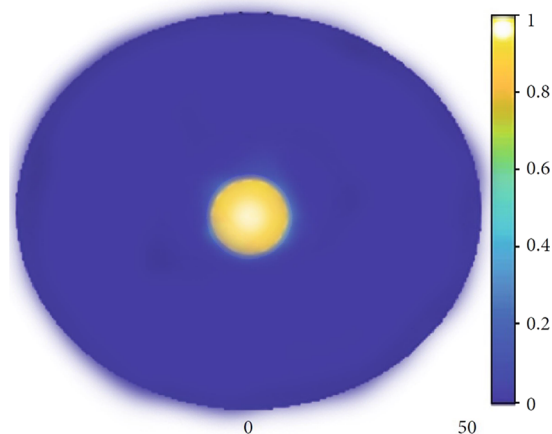
Figure 24. Reconstructed reference image.

images are similar to the expected image. Therefore, the similarity index can be used by evaluating the images' brightness, contrast, and structure.

Further details about the similarity index can be found in ref 59. All figures (Figures 11−23) listed in Table 2 are related to the images obtained with a 16 elements system. It is noted that the reconstructed images using the RTR algorithm have the most significant similarity index.

Table 3 compares the proposed imaging system's ability with other systems that utilized MWI and US techniques. The proposed system offered a high similarity between the

Table 2. Reconstructed Images' MSE and SSI Comparisons

images	MSE	SSI
Figure 11a	755.11	0.5775
Figure 11b	295.23	0.6756
Figure 11c	458.56	0.8721
Figure 11d	110.56	0.9898
Figure 12a	139.15	0.9799
Figure 12b	194.56	0.9579
Figure 13	120.57	0.9843
Figure 22	240.35	0.9212
Figure 14	230.48	0.9074
Figure 15	190.23	0.9487
Figure 18a	120.22	0.9887
Figure 18b	120.58	0.9798
Figure 19	140.32	0.9623
Figure 20	135.25	0.9743
Figure 21	178.36	0.9178
Figure 23	220.23	0.9478

Table 3. Recommended System, Compared with Recent Alike, Perform

references	techniques	trunk max radius (cm)	hollow min radius (mm)
25	MWI	15	25
26	MWI	15	25
38	MWI	11.5	30
60	US	12.5	11.8
61	US	(cube) $49.5 \times 30.1 \times 14.5$ cm^3	(rectangular area) 75×43 mm^2
62	US	15	12.5
proposed	MWI	15	2.75

reconstructed image and the actual or reference image, which was a circular target at the center of the trunk. In addition, the proposed system was compared with some similar systems shown in Table 3. Table 3 shows that the proposed method could detect a smaller target with the same trunk diameter as those systems. Furthermore, the proposed system detected a target (void) diameter much smaller than they achieved. Therefore, it could be concluded that the proposed approach offers much better results than theirs. It can be observed that the proposed system can attain superior outcomes in terms of resolution, and it provides detection of the smallest in different positions in the imaging media.

4.4. Reliability of the System and Repeatability of the Results. The consistency of the measurement data over numerous measurements, or the size of the measurement error concerning the inherent variability in the "error-free", "true", or underlying level of the quantity between subjects, are two definitions of dependability or accuracy.[63,64] The more significant error gives less reliability. Therefore, the reliability will be low if errors in reconstructed images are substantial compared to the reference images. The reliability of an instrument was determined using standard deviation (SDS) and measurement error, as presented in ref 64. Reliability has a value between zero and one. The value of one means no error exists in the results, and the value of zero represents an entirely incorrect result or 100% error. Furthermore, repeatability measures differences in the obtained data in multiple trials performed on the same sample.

The reliability inquiry and computation must be accomplished in a suitably nominated trial, assuming no less than two extents per subject under the same situations or media. A similar rater (variable) should be used. Besides, repeatability indicates how much agreement exists among the measurement results of the same subject, carried out under certain conditions. Its conditions consist of test results that are not dependent and obtained with the same method, on similar test subjects, in the same environment, or by the same operator, and using the same equipment. Thus, repeatability reflects the best achievable internal precision. The results can be indicated in terms of SD, coefficient of variation (CV), or relative standard deviation (RSD). The SSI is considered an output parameter under the same measurement method and similar conditions to analyze our imaging system's reliability, repeatability, and reproducibility. This analysis is performed for simulated and measured data for different sample dimensions. Therefore, we have two sets of values, one for the simulation data and another for the measurement data.

Two columns of 4 rows (four × two matrices) (Table 4) are considered for each simulated and measured data, those that have the nearest conditions in terms of the trunk and void diameters (dia). Figure 25 depicts both simulated and measured results along with the mean line (solid line), upper

Table 4. Input Data for Reliability and Repeatability Evaluation

simulation	measurement
97.75	98.33
96.25	99.10
99.78	98.38
99.21	98.65
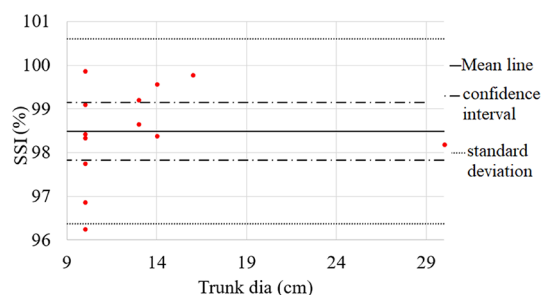
Figure 25. Simulated and measured SSI, their mean, CI, and SD lines.

and lower confidence interval (CI) (dashed line), and ±1.96 standard deviations (SD) (dotted line). The repeatability is nearly 100%, which is more than 98%. In addition, the experiment was performed in a laboratory environment first and then taken to the plantation. Changing the ports and connecting to VNA are done manually. Therefore, the repeatability might be a little less than 100%. A switch network can change the ports and get the received signals to get 100% repeatability.

Then, the "single ANOVA (analysis of variance)" and "descriptive statistics" were calculated in a Microsoft Excel spreadsheet to obtain the values needed to define the reliability and repeatability of these two groups of data. The single ANOVA gives us the sum squares (SS) within and between groups, degrees of freedom (df), mean square (MS), P-value, and F critical value. In addition, the descriptive statistics give us the standard error, SD, and 95% CI. The upper and lower CI can be calculated by adding to the mean and deducting the results from the mean value. After obtaining the parameters in both the ANOVA test and descriptive statistics, the reliability and repeatability of the study can be determined.[65] The reliability of the system can be calculated from the following equations presented in ref 64:

$$\frac{(\text{SD of subject's true values})^2}{(\text{SD of subject's true values})^2 + (\text{SD measurement error})^2}$$

$$= \frac{0.1243}{0.1243 + 0.031} = 0.8 = 80\% \tag{6}$$

The repeatability coefficient (RC) is investigated and considered to quantify the measurements carried out by a

single method or device under the same conditions. The same as reliability, the sample should be appropriately selected. The possibility of bias between every two observers in measurements was excluded in the repeatability study to start the evaluation. An alternate case can inform the SD of the discrepancies between two measurements completed on the identical subject.

$$\sqrt{2} \times \text{SD}_{\text{within subject}=0.49} \tag{7}$$

The estimated repeatability coefficient can be determined as follows:

$$1.96 \times \sqrt{2} \times \text{SD}_{\text{within subject}} = 0.977 \tag{8}$$

Suppose the differences between two measurements made on a subject are normally distributed, it will be expected that that variation between two measurements does not vary further than the repeatability constant in 95% of incidents. It means that the differences between any future measurement data by a particular observer and unit are approximated to be no more than 0.97 on 95% of occasions.[62]

As mentioned, the one-way ANOVA can be utilized to approximate the within-subject SD. However, the RC calculation is an estimation; thus, it is necessary to compute a CI to specify how it is approximated. Such a CI can be identified for RC as $1.96 \times \sqrt{2}$ (−1, 8.47).

First, the dataset should be plotted. The simplest one is to plot the subjects' measurements compared to the simulated one (or contrariwise). The points would be on the equality line if they showed no error. Overlaying the equality line can be applied to inspect if a bias exists to understand the differences between the simulation data and the measured ones (readers 1 and 2). Figure 26 shows the line of equality, the line of mean differences (solid line), the upper and lower limit of CI (dotted lines), and the lines that show the mean ±1.96SD (dashed lines).
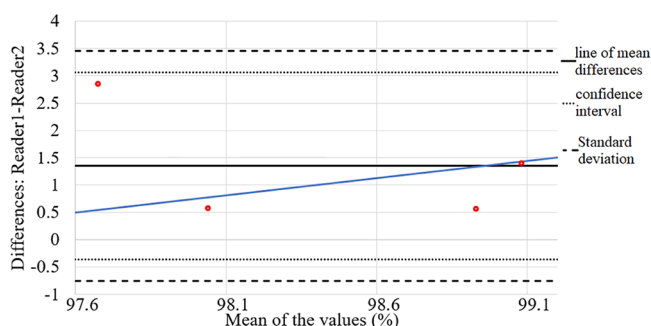
Figure 26. Differences between the simulated and measured SSI.

The system's stability is assumed on how much the output's lowest and the highest percentage values vary. Besides, it shows how various the simulated and measured graphs are.[66] Based on the ANOVA and the descriptive evaluation, the SSI results (both simulated and measured) obtained from different conditions show a slight and negligible variation between each group and within groups. Hence, system stability can be concluded.

5. CONCLUSIONS

Tropical trees are essential to most Asian countries' economies, especially their wood/timber industry. For instance, the rubber trees' health has been affected by a fungus that damages the tree's trunk and creates voids in the form of holes inside it. The presence of these voids in the tree trunk degenerates its productivity and ultimately destroys it. If the examination of the tree's health during the implementation is not performed correctly, monitoring its health during its productivity period will be necessary. Hence, there is a great interest in finding noninvasive imaging methods to monitor the health of the trees. Numerous imaging techniques have been recommended in the past. MWI has shown promising outcomes among various imaging techniques with a minimum tree invasion. This work established a noninvasive imaging system to identify voids in rubber trees at their early stage. The proposed UWB antenna array showed good efficiency and performance while placed on the surface of the tree trunks. We tested the array in two settings, planar and cylindrical arrangements. We examined the efficacy of the system through several tests. With high precision, voids as tiny as 4 mm were discovered in the reconstructed pictures, either in the center or off-center of 3D-printed samples of 16 and 30 cm diameter tree trunks. We used an improved time-reversal imaging algorithm to reconstruct the image of the void within the asymmetrical models. Eight 3D-printed samples were tested, four of which had no voids and four of which did. These eight samples included two voids with a diameter of 4 mm in the center, two with three voids with diameters of 3 mm in the center, and two asymmetrical samples with larger dimensions, one defective with a hole inside.

The proposed system showed robust performance through both simulation and measurement, and the improved algorithm was able to identify a void with a minimum diameter of 5.5 mm (the range, cross-range, and spatial resolution are ~6.5, ~8.5, and ~5.5 mm, respectively) and a maximum trunk diameter of 30 cm. The voids can be placed at different locations within the trunk. After investigating the system through simulation and measurement of 3D-fabricated samples, a lengthy sample of a rubber-wood trunk with a length of 75 cm was obtained and cut into smaller pieces to test the system's capabilities in detecting voids in a realistic setup. The reconstructed images of these wood samples also showed the excellent performance of the system and its accuracy in detecting and locating the voids. The antenna system and the applied algorithm could perfectly detect the hollow in both simulation and measurement setups (the asymmetric samples, both printed one and the actual trunk). Therefore, it can be applied for asymmetric and irregular samples other than a trunk. More antennas can be utilized in the system if a trunk with a bigger diameter is tested. The diameter of the trunk can be increased, and the system is capable of the detection of any voids in a bigger trunk. Only more antenna arrays should be used to cover all sections of the trunk or the antenna's beam width can be improved and make it wider; thus, no extra antenna will be required. In addition, the SSI examination depicted that the proposed imaging system attains tremendous significance compared to agarwood imaging in the literature. The proposed approach provides a significant resolution (compared with a current imaging system of wooden media using ultrasound technique), is highly reliable, and provides repeatable results. The 3D image reconstruction of the voids in the trunk is considered for the future work. The same antenna system and microwave imaging principles that were applied to reconstruct the 2D images of the void can also be used to

reconstruct the 3D image of the void; only more programming is required.

■ AUTHOR INFORMATION

Corresponding Author

Tale Saeidi − *Electrical and Electronics Engineering Department, Faculty of Engineering and Natural Sciences, İstinye University, Istanbul 34010, Turkey;* ● orcid.org/0000-0002-0995-3364; Email: talecommunication@gmail.com

Authors

Adam R. H. Alhawari − *Electrical Engineering Department, College of Engineering, Najran University, Najran 66462, Kingdom of Saudi Arabia*

Idris Ismail − *Electrical and Electronic Engineering Department of Universiti Teknologi PETRONAS, Bandar Seri Iskandar, Perak 32610, Malaysia*

Turki Alsuwian − *Electrical Engineering Department, College of Engineering, Najran University, Najran 66462, Kingdom of Saudi Arabia*

Ahmed Jamal Abdullah Al-Gburi − *Department of Electronics and Computer Engineering (FKEKK), Center for Telecommunication Research and Innovation (CeTRI), Universiti Teknikal Malaysia Melaka (UTeM), Durian Tunggal, Malacca 76100, Malaysia*

Complete contact information is available at:
https://pubs.acs.org/10.1021/acsomega.2c07015

Notes

The authors declare no competing financial interest.

■ REFERENCES

(1) Pornsuriya, C.; Sunpapao, A.; Srihanant, N.; Worapattamasri, K. A survey of diseases and disorders in oil palms of southern Thailand. *Plant Pathol. J.* **2013**, *12*, 169−175.

(2) Naher, L.; Yusuf, U. K.; Tan, S. G.; Ismail, A. Ecological status of Ganoderma and basal stem rot disease of oil palms (Elaeis guineensis Jacq.). *Aust. J. Crop Sci.* **2013**, *7*, 1723−1727.

(3) Hushiarian, R.; Yusof, N. A.; Dutse, S. W. Detection and control of Ganoderma boninense: strategies and perspectives. *Springerplus* **2013**, *2*, 555.

(4) Rebitanim, N. A.; Hanafi, M. M.; Idris, A. S.; Abdullah, S. N. A.; Mohidin, H.; Rebitanim, N. Z. Ganocare improves oil palm growth and resistance against Ganoderma basal stem rot disease in nursery and field trials. *Biomed Res. Int.* **2020**, *2020*, No. 3063710.

(5) Ramadiani, M. S.; Ramadhani, M. L.; Jundillah, M. L.; Azaini. Rubber plant disease diagnostic system using technique for order preference by similarity to ideal solution. *Procedia Comput. Sci.* **2019**, *161*, 484−492.

(6) Mazlan, S.; Jaafar, N. M.; Wahab, S.; Sulaiman, Z.; Rajandas, H.; Zulperi, D. Major diseases of rubber (hevea brasiliensis) in Malaysia. *Pertanika J. Sch. Res. Rev.* **2019**, *5*, 10−21.

(7) Jusoff, K.; Yusoff, M. H. M. New approaches in estimating rubberwood standing volume using airborne hyperspectral sensing. *Mod. Appl. Sci.* **2009**, *3*, 62−70.

(8) Imran, S. N. M.; Baharudin, F.; Ali, M. F.; Rahiman, M. H. F. Chemical relationship on detection of Ganoderma disease on oil palm tree system. *Earth Environ. Sci.* **2018**, *140*, No. 012048.

(9) Bivi, M. S. H. R.; Paiko, A. S.; Khairulmazmi, A.; Akhtar, M. S.; Idris, A. S. Control of basal stem rot disease in oil palm by supplementation of calcium, copper, and salicylic acid. *Plant Pathol. J.* **2016**, *32*, 396−406.

(10) Bucur, V., *Non-destructive characterization and imaging of wood'*; Springer Series in Wood Science: 54280 Champenoux, France, 2003.

(11) Arciniegas, A.; Prieto, F.; Brancheriau, L.; Lasaygues, P., *"Literature review of acoustic and ultrasonic tomography in standing trees*; Springer-Verlag Berlin Heidelberg, 2014, *28*, 1559−1567.

(12) Hasenstab, A.; Krause, M.; Osterloh, K., *"Testing of wooden construction elements with ultrasonic echo technique and x-ray"*; ECNDT, 2006.

(13) Wang, F.; Marashdeh, Q.; Fan, L. S.; Warsito, W. Electrical capacitance volume tomography: design and applications. *Sensors* **2010**, *10*, 1890−1917.

(14) Mayo, S. C.; Chen, F.; Evans, R. Micron-scale 3D imaging of wood and plant microstructure using high-resolution X-ray phase-contrast microtomography. *J. Struct. Biol.* **2010**, *171*, 182−188.

(15) Ashtari, A.; Noghanian, S.; Sabouni, A.; Aronsson, J.; Thomas, G.; Pistorius, S. Using a priori Information for Regularization in Breast Microwave Image Reconstruction. *IEEE Trans. Biomed. Eng.* **2010**, *57*, 2197−2208.

(16) Elwi, T. A.; Salim, A. J.; Alkhafaji, A. N.; Ali, J. K.; Jalal, A. S. A., *"Complex constitutive characterizations of materials in the x-band using a non-destructive technique,"* *Special Issue of the 8th International Advances in Applied Physics and Materials Science Congress (APMAS 2018)*; Acta Physica Polonica A, 2019, *135*.

(17) Elwi, T. A. Metamaterial based a printed monopole antenna for sensing applications. *Int. J. RF Microw. Comput.-Aided Eng.* **2018**, *28*, No. e21470.

(18) Imran, A. I.; Elwi, T. A. A cylindrical wideband slotted patch antenna loaded with Frequency Selective Surface for MRI applications. *Eng. Sci. Technol., Int. J.* **2017**, *20*, 990−996.

(19) Elwi, T. A. On the percentage quantization of the moisture content in the Iraqi petroleum productions using microwave sensing. *Al-Ma'mon Coll. J.* **2016**, *28*, 262−277.

(20) Noghanian, S.; Sabouni, A.; Desell, T.; Ashtari, A. *"Microwave Tomography: Global Optimization, Parallelization and Performance Evaluation"*; Springer: New York, 2014.

(21) Chuah, H. T.; Lee, K. Y.; Lau, T. W. Dielectric constants of rubber and oil palm leaf sample at x band. *IEEE Trans. Geosci. Remote Sens.* **1995**, *33*, 221.

(22) Marzinotto, M.; Santulli, C.; Mazzetti, C. Dielectric properties of oil palm-natural rubber biocomposites. *Annual Report Conference on Electrical Insulation and Dielectric Phenomena* **2007**, *1*, 584 −587.

(23) Elwi, T. A. Novel UWB printed metamaterial microstrip antenna based organic substrates for rf-energy harvesting applications. *AEU − Int. J. Electron. Commun.* **2019**, *101*, 44−53.

(24) Saeidi, T.; Ismail, I.; Wen, W. P.; Alhawari, A. R. H. Ultra-wideband elliptical patch antenna for microwave imaging of wood. *Int. J. Microw. Wireless Technol.* **2019**, *11*, 948−966.

(25) Effendi, M. R.; Willyantho, R.; Munir, A., *"Back propagation technique for image reconstruction of microwave tomography,"* *ICBET' 19: Proceedings 9th International Conference on Biomedical Engineering and Technology*; Association for Computing Machinery: New York, NY, United States, 2019.

(26) Boero, F.; Fedeli, A.; Lanini, M.; Maffongelli, M.; Monleone, R.; Pastorino, M.; Randazzo, A.; Salvadè, A.; Sansalone, A. Microwave tomography for the inspection of wood materials: imaging system and experimental results. *IEEE Trans. Microw. Theory Tech.* **2018**, *66*, 3497−3510.

(27) Pastorino, M.; Randazzo, A.; Fedeli, A.; Salvadè, A.; Maffongelli, M.; Monleone, R.; Lanini, M. A microwave tomographic system for wood characterization in the forest products industry. *Wood Mater. Sci. Eng.* **2015**, *10*, 75−85.

(28) Rahiman, M. H. F.; Thomas, T. W. K.; Soh, P. J.; Rahim, R. A.; Jamaluddin, J.; Ramli, M. F. Microwave tomography sensing for potential agarwood trees imaging. *Comput. Electron. Agric.* **2019**, *164*, No. 104901.

(29) Roggenbuck, M.; Catenacci, J.; Walker, R.; Hanson, E.; Hsieh, J.; Patch, S. K., "Thermoacoustic imaging with VHF signal generation: a new contrast mechanism for cancer imaging over large fields of view," Abdomen and Thoracic Imaging; Springer: US, 2014, 523−557.

(30) Hao, X.; Xiong, W.; Tao, Q.; Huan, M.; Yexian, Q.; Witte, R. S., "Time-efficient contrast-enhanced thermoacoustic imaging modality for 3-D breast cancer detection using compressive sensing," in General Assembly and Scientific Symposium (URSI GASS), 2014 XXXIth URSI, 2014, 1−2.

(31) Saeidi, T.; Ismail, I.; Mahmood, S. N.; Alani, S.; Alhawari, A. R. H. Microwave imaging of voids in oil palm trunk applying UWB antenna and robust time-reversal algorithm. J. Sens. 2020, 2020, No. 8895737.

(32) Sattar, Z. A., "Experimental analysis on effectiveness of confocal algorithm for radar-based breast cancer detection, "Online Available at: http://etheses.dur.ac.uk/3531/1/MSCR, 2012.

(33) Ahadi, M.; Isa, M.; Saripan, M. I.; Hasan, W. Z. W. Three dimensions localization of tumors in confocal microwave imaging for breast cancer detection. Microw. Opt. Technol. Lett. 2015, 57, 2917−2929.

(34) Li, X.; Hagness, S. C. A confocal microwave imaging algorithm for breast cancer detection. Microw. Wireless Comp. Lett., IEEE 2001, 11, 130−132.

(35) Bocquet, B.; van de Velde, J. C.; Mamouni, A.; Leroy, Y.; Giaux, G.; Delannoy, J.; Delvalee, D. Microwave radiometric imaging at 3 GHz for the exploration of breast tumors. IEEE Trans. Microw. Theory Tech. 1990, 38, 791−793.

(36) Stauffer, P. R.; Rodriques, D. B.; Salahi, S.; Topsakal, E.; Oliveira, T. R.; Prakash, A., "Stable microwave radiometry system for long term monitoring of deep tissue temperature", 2013, 85840R-85840R-11.

(37) Cano, J. D. G.; Fasoula, A.; Duchesne, L.; Bernard, J. G. Wavelia breast imaging: the optical breast contour detection subsystem. Appl. Sci. 2020, 10, 1234.

(38) Brancaccio, A.; Dell'Aversano, A.; Leone, G.; Solimene, R. Subsurface detection of shallow targets by undersampled multi-frequency data and a non-cooperative source. Appl. Sci. 2019, 24, 5383.

(39) Taflove, A.; Hagness, S. C., "Computational electrodynamics: the finite- difference time-domain method," 2nd ed.; Artech House: Norwood, MA, 2000.

(40) Elahi, M. A.; O'Loughlin, D.; Lavoie, B. R.; Glavin, M.; Jones, E.; Fear, E. C.; O'Halloran, M. Evaluation of image reconstruction algorithms for confocal microwave imaging: application to patient data. Sensors 2018, 18, 1678.

(41) Jacobsen, S.; Birkelund, Y. Improved resolution and reduced clutter in ultra-wideband microwave imaging using cross-correlated back projection: experimental and numerical results. Int. J. Biomed. Imaging 2010, 2010, 1.

(42) Thomas, J. L.; Fink, M. A. Ultrasonic beam focusing through tissue inhomogeneities with a time-reversal mirror: application to transskull therapy. IEEE Trans. Ultrason. Ferroelectr. Freq. Control 1996, 43, 1122−1129.

(43) Fink, M. Time reversal of ultrasonic fields. I. Basic principles. IEEE Trans. Ultrason. Ferroelectr. Freq. Control 1992, 39, 555−566.

(44) Liu, D.; Kang, G.; Li, L.; Chen, Y.; Vasudevan, S.; Joines, W.; Liu, Q. H.; Krolik, J.; Carin, L. Electromagnetic time-reversal imaging of a target in a cluttered environment. IEEE Trans. Antenna Propag. 2005, 53, 3058−3066.

(45) Mukherjee, S.; Tamburrino, A.; Haq, M.; Udpa, S.; Udpa, L. Far-field microwave NDE of composite structures using time-reversal mirror. NDT E Int. 2018, 93, 7−17.

(46) Kosmas, P.; Rappaport, C. M. Time reversal with the FDTD method for microwave breast cancer detection. IEEE Trans. Microw. Theory Tech. 2005, 53, 2317−2323.

(47) Akinci, M. N.; Çayören, M.; AkduFman, I. Near-field orthogonality sampling method for microwave imaging: Theory and experimental verification. IEEE Trans. Microw. Theory Tech. 2016, 64, 2489−2501.

(48) Islam, M. M.; Islam, M. T.; Samsuzzaman, M.; Faruque, M. R. I.; Misran, N. Microstrip line-fed fractal antenna with a high-fidelity factor for UWB imaging applications. Microw. Opt. Technol. Lett. 2015, 57, 2580−2585.

(49) Mukherjee, S.; Udpa, L.; Udpa, S.; Rothwell, E. J.; Deng, Y. A time reversal-based microwave imaging system for detection of breast tumors. IEEE Trans. Microw. Theory Tech. May 2019, 67, 2062.

(50) Mukherjee, S.; Udpa, L.; Udpa, S.; Rothwell, E. J. Target localization using microwave time-reversal mirror in reflection mode. IEEE Trans. Antennas Propag. 2017, 65, 820−828.

(51) Kabir, M. F.; Daud, W. M.; Khalid, K.; Sidek, H. A. A. Dielectric and ultrasonic properties of rubber-wood. Effect of moisture content, grain direction and frequency. Holz Roh- Werkst. 1998, 56, 223−227.

(52) Lamensdorf, D.; Susman, L. Baseband-pulse-antenna techniques. IEEE Antennas Propag. Mag. 1994, 36, 20−30.

(53) https://www.sciencedirect.com/topics/engineering/cross-range resolution.

(54) Li, H.-J.; Liu, T.-Y.; Yang, S. H. Superhigh image resolution for microwave imaging. Int. J. Imaging Syst. Technol. 1990, 2, 37−46.

(55) Simonov, N.; Son, S. H.; Kim, B. R.; Jeon, S. Investigation of spatial resolution in a microwave tomography system; Radio Technology Research Department, ETRI, 2012, 12 (1), 107 −114.

(56) Simonov, N. A.; Jeon, S. I.; Son, S. H.; Lee, J. M.; Kim, H. J., "About Equivalency of Two Methods of Information Gathering in Microwave Imaging," 2012 International Symposium on Antennas and Propagation (ISAP), IEEE, Nagoys, Japan, Dec 2012.

(57) https://all3dp.com/2/wood-filament-for-a-3d-printer-explained-compared/.

(58) Saeidi, T.; Ismail, I.; Wen, W. P.; Alhawari, A. R. H. Dielectric properties of complete oil palm trunk sample (healthy and unhealthy). AIP Adv. 2019, 9, No. 075314.

(59) Wang, Z.; Bovik, A. C.; Sheikh, H. R., "Structural Similarity Based Image Quality Assessment," Chapter 7 in Digital Video Quality and Perceptual Coding; Marcel Dekker Series in Signal Processing and Communications, 2005.

(60) Arciniegas, A.; Brancheriau, L.; Gallet, P.; Lasaygues, P., "Device for ultrasound imaging of standing trees"; Acoustical Society of America through the American Institute of Physics, 2013, 19.

(61) Krause, M.; Mayer, K.; Chinta, P. K.; Effner, U. Ultrasonic imaging of defects in building elements made from timber. Adv. Mater. Res. 2013, 778, 312−320.

(62) Espinosaa, L.; Prieto, F.; Brancheriau, L.; Lasaygues, P. Quantitative parametric imaging by ultrasound computed tomography of trees under anisotropic conditions: Numerical case study. Ultrasonics 2020, 102, No. 106060.

(63) https://radiologykey.com/measurements-validity-reliability-and-responsiveness/

(64) Bartlett, J. W.; Frost, C. Reliability, repeatability and reproducibility: analysis of measurement errors in continuous variables. Ultrasound Obstet. Gynecol. 2008, 31, 466−475.

(65) https://www.webassign.net/question_assets/unccolphysmechl1/measurements/manual.html

(66) Yadav, P.; Tolakanahalli, R.; Rong, Y.; Paliwal, B. R. The effect and stability of MVCT images on adaptive TomoTherapy. J. Appl. Clin. Med. Phys. 2010, 11, 4.